Petroleum Science 22 (2025) 1110–1124

Contents lists available at ScienceDirect

Petroleum Science

journal homepage: www.keaipublishing.com/en/journals/petroleum-science

Original Paper

An integrated method of data-driven and mechanism models for formation evaluation with logs

Meng-Lu Kang [a, b], Jun Zhou [a, b], Juan Zhang [a, b], Li-Zhi Xiao [a, b, *], Guang-Zhi Liao [a, b], Rong-Bo Shao [a, b], Gang Luo [a, b]

[a] State Key Laboratory of Petroleum Resources and Engineering, China University of Petroleum (Beijing), Beijing, 102249, China
[b] College of Artificial Intelligence, China University of Petroleum (Beijing), Beijing, 102249, China

ARTICLE INFO

Article history:
Received 24 January 2024
Received in revised form
16 October 2024
Accepted 15 January 2025
Available online 22 January 2025

Edited by Meng-Jiao Zhou and Min Li

Keywords:
Well log
Reservoir evaluation
Label scarcity
Mechanism model
Data-driven model
Physically informed model
Self-supervised learning
Machine learning

ABSTRACT

We propose an integrated method of data-driven and mechanism models for well logging formation evaluation, explicitly focusing on predicting reservoir parameters, such as porosity and water saturation. Accurately interpreting these parameters is crucial for effectively exploring and developing oil and gas. However, with the increasing complexity of geological conditions in this industry, there is a growing demand for improved accuracy in reservoir parameter prediction, leading to higher costs associated with manual interpretation. The conventional logging interpretation methods rely on empirical relationships between logging data and reservoir parameters, which suffer from low interpretation efficiency, intense subjectivity, and suitability for ideal conditions. The application of artificial intelligence in the interpretation of logging data provides a new solution to the problems existing in traditional methods. It is expected to improve the accuracy and efficiency of the interpretation. If large and high-quality datasets exist, data-driven models can reveal relationships of arbitrary complexity. Nevertheless, constructing sufficiently large logging datasets with reliable labels remains challenging, making it difficult to apply data-driven models effectively in logging data interpretation. Furthermore, data-driven models often act as “black boxes” without explaining their predictions or ensuring compliance with primary physical constraints. This paper proposes a machine learning method with strong physical constraints by integrating mechanism and data-driven models. Prior knowledge of logging data interpretation is embedded into machine learning regarding network structure, loss function, and optimization algorithm. We employ the Physically Informed Auto-Encoder (PIAE) to predict porosity and water saturation, which can be trained without labeled reservoir parameters using self-supervised learning techniques. This approach effectively achieves automated interpretation and facilitates generalization across diverse datasets.

1. Introduction

Formation evaluation is essential in exploring and developing oil and gas, with porosity and water saturation as critical reservoir parameters. As the oil and gas industry advances, the geological complexity encountered during research has escalated, leading to high demands for accurate prediction of reservoir parameters. Simultaneously, the costs associated with manual interpretation have surged, making precise interpretation and cost reduction particularly challenging. The most effective and accurate approach involves acquiring core samples during drilling, followed by laboratory-based physical analysis to determine reservoir parameters. However, this technique is not widely applicable due to elevated sampling and testing expenses. Furthermore, although accurate, the parameters derived from this method reflect only localized strata characteristics, impeding macroscopic analysis of subsurface geological formations.

In conventional logging data interpretation, empirical relationships between logging data and reservoir parameters are often employed as the basis for parameter determination. For example, the porosity (POR) interpretation model is typically constructed using density (DEN), neutron (CNL), and acoustic (AC) logs to

* Corresponding author.
E-mail address: xiaolizhi@cup.edu.cn (L.-Z. Xiao).

https://doi.org/10.1016/j.petsci.2025.01.004

determine POR quantitatively. Additionally, in Archie's formula (Archie, 1942, 1947), formation water saturation (SW) is resolved by combining formation resistivity (RT) and formation water resistivity (RW). While these mechanism models address logging data interpretation within specific ranges, they are applicable only under ideal conditions. The relationship between actual reservoir parameters and well logging data becomes complex and nonlinear in diverse geological conditions. Additionally, the manual interpretation is often inefficient and prone to subjective bias.

Artificial intelligence has provided innovative solutions to traditional logging data interpretation limitations. With access to substantial datasets and corresponding labels, data-driven machine learning offers the potential to establish complex mapping relationships (Xiao, 2022). The typical applications of intelligent logging data interpretation include reservoir parameters prediction (Shao et al., 2022a), lithology identification (Dong et al., 2023a), fluid identification (Luo et al., 2022; Gao et al., 2022), and fracture evaluation (Zhao et al., 2022). Contemporary research primarily utilizes models such as Long Short-Term Memory (LSTM) networks (Gers et al., 2000; Hochreiter and Schmidhuber, 1997) and Convolutional Neural Networks (CNN) (Lecun et al., 1998; Szegedy et al., 2015), which have been empirically demonstrated to effectively capture the nonlinear relationships between reservoir parameters and logging data, as well as the sequential relationships along the depth dimension. For instance, An et al. (2019) employed LSTM to predict clay content and porosity, achieving reductions of 42.2% and 48.6%, respectively, in prediction errors. Song et al. (2019) integrated CNN and Gated Recurrent Units (GRU) for porosity prediction, exhibiting localized perception capability and long-term memory capacity with the hybrid CNN-GRU model. Wang et al. (2020) used a Copula function-based correlation analysis for dimensionality reduction of logging data, selecting susceptible features as inputs for a GRU network designed for reservoir parameters prediction. Liao et al. (2020) applied data mining and clustering algorithms to categorize porosity structures, utilizing a CNN model to predict microscopic reservoir pore structures based on core capillary pressure data. Luo et al. (2022) proposed a parallel network combining LSTM and CNN, effectively enabling multi-level reservoir fluid identification. This approach improved the accuracy of identifying oil-bearing reservoirs and enhanced the distinction between closely related reservoirs.

To further improve the accuracy of logging data interpretation, algorithm design and model architecture advancements have driven the development of ensemble learning, transfer learning, and multitask learning. Tang et al. (2021) proposed an ensemble learning framework based on gradient-boosted decision trees (GBDTs) to improve the agreement rate of sweet spot identification. In the context of lithology recognition, Dong et al. (2023b) further examined the application of ensemble learning, exploring subclassifier selection strategies to optimize performance. Shao et al. (2022a) introduced transfer learning for reservoir parameter prediction by transferring specific parameters from a jointly trained porosity and water saturation model to a permeability prediction model. Building on this approach, Shao et al. (2022b) proposed an innovative cross-architecture multitask reservoir parameter prediction model, where the private layer architecture can be individually designed for each reservoir parameter. Both models leverage the correlation effect between reservoir parameters.

Nevertheless, these data-driven models face several challenges in practical application. Firstly, training labels are usually derived from traditional logging data interpretation, which is inherently multi-interpretable and uncertain, introducing bias. Secondly, data-driven models often lack interpretability, resembling “black boxes” whose prediction rationale remains opaque. Interpretability to machine learning models. Given the limitations of current data-driven models, researchers have highlighted fundamental challenges in AI development. Karniadakis et al. (2021) emphasized combining machine learning with physical laws, especially in partial data and insight scenarios, to enhance generalization and alignment with fundamental principles. Similarly, Xiao (2022) argued that deep learning relies on simple network rules and computational power lacks interpretability, suggesting a need for models that merge mechanisms and data-driven approaches for greater transparency.

Current research on integrating mechanism and data-driven models follows two approaches. The first approach involves modifying the architecture of machine learning models to ensure that the predictions inherently conform to physical principles. For instance, Chen and Zhang (2020) adjusted a network based on a mechanism model for calculating geological parameters by adding two neurons to the hidden layer to emulate the underlying physical mechanisms, thereby constructing a physically constrained LSTM network model. The second approach embeds physical knowledge into model predictions by imposing constraints, which can be categorized into soft and hard constraints. Soft constraints are implemented through loss functions that penalize deviations of predictions from specified physical principles, ensuring that the model's outputs approximately satisfy these constraints. For example, Doan et al. (2020) proposed an echo state network (ESN) grounded in physical principles, introducing a system control equation within the loss function to penalize predictions misaligned with physics. Similarly, Rao et al. (2020) incorporated residual physics equations into the loss function to construct a physics-informed neural network (PINN), which was applied to simulate steady and transient laminar flows at low Reynolds numbers. In the context of fracture evaluation, PINNs have been used to predict rock mechanical parameters such as modulus of elasticity, Poisson's ratio, tensile strength, and fracture toughness, with empirical formulas and boundary conditions embedded in the loss function through automatic differentiation (Li et al., 2023). On the other hand, hard constraints ensure the strict satisfaction of given physical equations within specific domains. Theoretically, hard constraints enable higher prediction accuracy with fewer data points and enhance robustness. Chen et al. (2021) introduced the Hard Constraint Projection (HCP) model, which converts control equations and physical constraints into discretizable forms, optimizing hard constraints through projection. Empirical evidence suggests this method is more effective and exhibits superior extrapolation capabilities compared to traditional soft constraint approaches.

However, whether embedding the mechanism model in the model structure or the learning criteria, the data-driven component primarily relies on label-driven mechanisms, ultimately seeking a balance between the labels and mechanism models. Consequently, the accuracy of labels is crucial during the training process. Obtaining core data is challenging in geophysical scenarios, and labels derived from interpretation introduce subjective elements. Therefore, it is necessary to reduce the dependence on labels further.

This paper proposes an integrated method of data-driven and mechanism models for well logging formation evaluation called Physically Informed Auto-Encoder (PIAE). The self-supervised framework of PIAE reduces the model's reliance on data quality and quantity by seeking a balance between actual well logging data and mechanism models, thereby avoiding the errors introduced by manual interpretation labels. PIAE embeds the mechanism models into the neural network architecture, with only the structure of the mechanism model being constrained. Additionally, it effectively integrates domain knowledge into the training process and the loss function, allowing for the optimization of mechanism parameters

within a reasonable range. This approach effectively automates the interpretation process and enhances generalization across diverse datasets.

2. Methodology

2.1. PIAE method

This paper proposes the PIAE method integrating data-driven and mechanism models for well logging formation evaluation. Data-driven models are incorporated as encoders using LSTM, CNN, and MLP. While mechanism models, including the multi-mineral volume model and Archie's formula, are designed as decoders. The model is a parallel integration of two auto-encoders, denoted as P1 and P2 in Fig. 1. Both parts encompass a sequential integration of data-driven and mechanism models. Therefore, the PIAE architecture represents a hybrid integration of data-driven and mechanism models.

The PIAE framework consists of multi-mineral volume encoder $e_{\mathrm{M}}(x;\theta)$, multi-mineral volume decoder $d_{\mathrm{M}}(x;\rho)$, Archie encoder $e_{\mathrm{A}}(x;\varphi)$ and Archie decoder $d_{\mathrm{A}}(x)$, where θ, ρ, ϕ are trainable parameters of modules. The forward propagation of PIAE is shown in Eqs. (1)–(7).

$$v = e_{\mathrm{M}}(x), \quad e_{\mathrm{M}}(x;\theta) : \mathbb{R}^{W\times N} \to \mathbb{R}^{M} \tag{1}$$

$$y_1 = d_{\mathrm{M}}(v), \quad d_{\mathrm{M}}(x;\rho) : \mathbb{R}^{M} \to \mathbb{R}^{N-1} \tag{2}$$

$$\mathrm{POR} = v_{M-1} + v_M \tag{3}$$

$$\mathrm{SW} = v_{M-1}/\mathrm{POR} \tag{4}$$

$$mn = e_{\mathrm{A}}\left(\left[x^4; x^5\right]\right), \quad e_{\mathrm{A}}(x;\varphi) : \mathbb{R}^{W\times 2} \to \mathbb{R}^{2} \tag{5}$$

$$y_2 = d_{\mathrm{A}}([\mathrm{POR}, \mathrm{SW}, mn]), \quad d_{\mathrm{A}}(x) : \mathbb{R}^{4} \to \mathbb{R}^{1} \tag{6}$$

$$y = \mathrm{Norm}([y_1, y_2]) \tag{7}$$

where $\mathrm{Norm}(\cdot)$ denotes normalization of vectors and $[\cdot,\cdot]$ denotes concatenation of vectors.

The input $x = [x^1, x^2, \cdots x^N] \in \mathbb{R}^{W\times N}$ is constructed by window slicing based on measured logging data, including density log (DEN), compensated neutron log (CNL), acoustic log (AC), gamma ray (GR), and formation resistivity (RT). The output $y \in \mathbb{R}^N$ is the corresponding reconstructed logging data (DEN*, CNL*, AC*, GR*, RT*), used as supervision term in L_{data}. The training objective aims to minimize the loss function formed by L_{data} and L_{mn}.

In P1, the slicing feature $x \in \mathbb{R}^{\mathrm{W}\times\mathrm{N}}$ is encoded by e_{M} to mineral volume content $v \in R^M$, which is subsequently decoded by d_{M} to reconstructed logging data $y_1 \in \mathbb{R}^{N-1}$ excluding RT*. Furthermore, volume content of water v_{M-1} and oil v_M are further utilized to compute POR and SW. In P2, encoder e_{A} takes x^{N-1} and x^N as inputs, representing the slicing feature of RT and GR, respectively. The rock-electrical parameter vector $mn \in \mathbb{R}^2$, which is the output of e_{A}, are concatenated with POR and SW. The concatenated vector serves as input to d_{A}, which decodes it into the output $y_2 \in \mathbb{R}^1$ representing RT*. The outputs of P1 and P2 are concatenated and then normalized to obtain the final output $y \in \mathbb{R}^N$. In this paper, the window size W is 21, the original feature length N is 5 and the quantity of mineral components M is 9.

2.1.1. Multi-mineral volume encoder

The multi-mineral encoder e_{M} is designed as a parallel structure of CNN and LSTM, which facilitates the extraction of complex correlations between logging data and reservoir parameters. These foundational models are selected based on their widespread use and demonstrated effectiveness in interpreting logging data (Luo et al., 2022; Song et al., 2019).

CNN comprises convolutional layers, pooling layers, and fully connected layers (Lecun et al., 1998; Szegedy et al., 2015). The convolutional layers extract features from the data, where multiple convolutional kernels are set to capture distinct features within the data. Pooling layers perform subsampling on the features extracted by the convolutional layers to reduce overfitting. The resulting features are then flattened into a vector and fed into fully connected

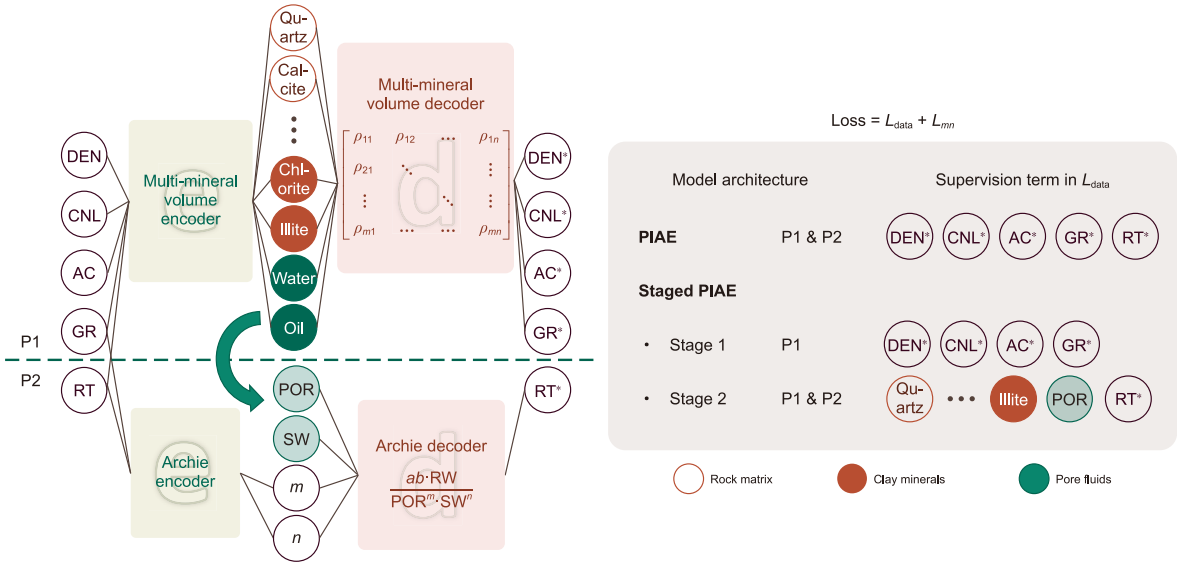

Fig. 1. The overall structure of PIAE and staged PIAE.

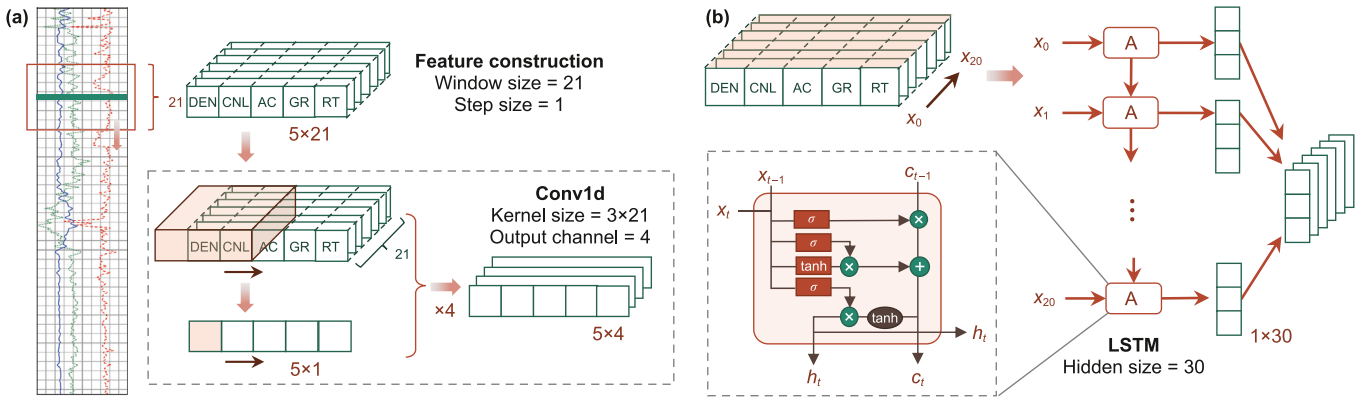

Fig. 2. The principle of 1-D convolution layer and LSTM layer.

layers for specific tasks. As illustrated in Fig. 2(a), the 1-D convolution process in logging data involves sliding convolution kernels over constructed features to learn the correlations between logging data. Multiple convolution kernels slide simultaneously to learn different features within the logging data.

LSTM is a recurrent neural network (RNN) adept at handling sequential data and maintaining long-term dependencies (Gers et al., 2000; Hochreiter and Schmidhuber, 1997). It is achieved by incorporating memory cells and gated units, including input gates, forget gates, and output gates. Fig. 2(b) illustrates the structure of memory cells and the LSTM layer. For time step t, the input of the LSTM layer includes C_{t-1}, h_{t-1} and x_t, represent the cell state at time $t-1$, the hidden state at time $t-1$, and the input vector at time t, respectively. The output comprises the cell state C_t and hidden state h_t at time t. In typical layered rock formations, the formation order determines the strata's superimposition relation, which is reflected in well-log curves as a sequential relationship in the depth direction. Therefore, LSTM can effectively process logging data by capturing temporal relationships between measurements at different depths.

By integrating CNN and LSTM as a parallel structure, the multi-mineral encoder leverages the strengths of both types of models. Leveraging the local perception capacity of CNN, 1-D convolution is employed to extract correlations in the feature dimension. Meanwhile, the memory capacity of the LSTM network is utilized to capture temporal information in the depth dimension. Table D.1 and Table D.2 show the specific setting of multi-mineral encoder architecture.

2.1.2. Multi-mineral volume decoder

The multi-mineral volume model is a linear logging response equation, typically serving as the mechanism model for formation evaluation. Various rock components, including rock matrix, clay minerals, and pore fluids, are assumed to possess distinct mineral volumes in the formation. The sum of all mineral volumes within the formation equals 1. Eqs. (8) and (9) represent the response equation of the formation to logging data. Involving n logging curves and m types of minerals, the multi-mineral volume model can be formulated in matrix form (Yong and Zhang, 2007).

$$\begin{bmatrix} v_1 \\ v_2 \\ \vdots \\ v_m \end{bmatrix}^{\mathrm{T}} \begin{bmatrix} \rho_{11} & \rho_{12} & \cdots & \rho_{1n} \\ \rho_{21} & \ddots & & \vdots \\ \vdots & & \ddots & \vdots \\ \rho_{m1} & \cdots & \cdots & \rho_{mn} \end{bmatrix} = \begin{bmatrix} y_1 \\ y_2 \\ \vdots \\ y_n \end{bmatrix}^{\mathrm{T}} \tag{8}$$

$$\sum_i v_i = 1 \tag{9}$$

In the multi-mineral volume decoder d_{M}, the linear logging response equation is transformed into neural network layers. The linear logging response Eq. (8) is considered a fully connected layer without bias, where v_i represents the input neurons, y_i represents the output neurons, and the coefficient matrix composed of mineral response parameters represents the weight of the linear layer. Minerals with relatively higher component content are selected as candidates through clay mineral and rock slice analysis of the studied region. Ultimately, the mineral components are determined to be quartz, calcite, mica, chlorite, illite, kaolinite, montmorillonite, water, and oil. The specific coefficient matrix is described in Table A.1. The initialized weight parameters ρ undergo maximum and minimum normalization by Eq. (10) to achieve a consistent updating scale during backpropagation. Consequently, the normalized output y' is derived following Eq. (11).

$$\rho'_{m\times n} = \begin{bmatrix} \dfrac{\rho_{11} - \min\limits_{1j}(\rho_{1j})}{\max\limits_{1j}(\rho_{1j}) - \min\limits_{1j}(\rho_{1j})} & \cdots & \dfrac{\rho_{1n} - \min\limits_{1j}(\rho_{1j})}{\max\limits_{1j}(\rho_{1j}) - \min\limits_{1j}(\rho_{1j})} \\ \vdots & \ddots & \vdots \\ \dfrac{\rho_{m1} - \min\limits_{1j}(\rho_{mj})}{\max\limits_{mj}(\rho_{mj}) - \min\limits_{1j}(\rho_{mj})} & \cdots & \dfrac{\rho_{mn} - \min\limits_{1j}(\rho_{mj})}{\max\limits_{mj}(\rho_{mj}) - \min\limits_{1j}(\rho_{mj})} \end{bmatrix} \tag{10}$$

$$y' = v^{\mathrm{T}}\rho' \tag{11}$$

The final output y is obtained by reverse normalization and restoration to the original scale.

$$y = \begin{bmatrix} y'_1 \cdot \left(\max\limits_{1j}(\rho_{1j}) - \min\limits_{1j}(\rho_{1j}) \right) + \min\limits_{1j}(\rho_{1j}) \\ \vdots \\ y'_n \cdot \left(\max\limits_{1j}(\rho_{1j}) - \min\limits_{1j}(\rho_{1j}) \right) + \min\limits_{1j}(\rho_{1j}) \end{bmatrix}^{\mathrm{T}} \tag{12}$$

The mass balance equation in Eq. (9) constrain the sum of all mineral volume content to be 1. Similarly, The Softmax function, as shown in Eq. (13), is a commonly used activation function in neural networks. It maps the outputs of multiple neurons to a probability distribution within the range of 0–1 and constrain the sum of the outputs to be 1.

$$\mathrm{Softmax}(v_i) = e^{v_i} \Big/ \sum_{m=1}^{M} e^{v_m} \tag{13}$$

Therefore, the same constraining effect is achieved by

introducing Softmax as an activation function after the input layer neurons of a fully connected layer. The linear logging response equation is successfully embedded into the neural network.

2.1.3. Archie encoder and Archie decoder

Archie's formula is an empirical equation used for calculating water saturation (Archie, 1942) according to Eq. (14).

$$\mathrm{SW} = \left(\frac{ab \cdot \mathrm{RW}}{\mathrm{RT} \cdot \mathrm{POR}^m}\right)^{\frac{1}{n}} \tag{14}$$

where RW is the formation water resistivity obtained through formation water analysis, and a, b, m, and n are regression parameters from rock-electrical experiments. Among them, a and b are lithology-related coefficients, m is the cementation index, and n is the saturation exponent.

The rock-electro parameters a, b, m, and n will yield uniform values for the experimental rock samples because they are obtained through regression using experimental data. Consequently, for rock samples of the same lithology but with different porosities, Archie's formula requires identical values of a, b, m, and n; otherwise, discrepancies arise (Sun, 2007; Yang et al., 2018). For reservoirs in different conditions, researchers have conducted a series of investigations and improvements on Archie's formula, including distinct parameter selections, simplification and enhancement of the equation's form, and the introduction of other pertinent variables (Haro, 2010; Kennedy and Herrick, 2012; Zhang, 2020). In practice, there are several limitations to Archie's formula. One of these is the omission of the influence of clay content on conductivity within the rock matrix and assuming the matrix to be an insulator. Some studies have indicated that the response equation for clay-bearing sandstone aligns with pure sandstone, differing only in rock electrical parameters (Han and Pan, 2010; Yang et al., 2018).

Therefore, considering the effects of clay content, variable rock-electro parameters are employed in Archie's formula. The rock-electro parameters are treated as outputs of e_{A}, which is constructed as MLP with four hidden layers. The logging data RT and GR are inputs to e_{A}, with m and n as outputs. The specific structure of e_{A} is detailed in Table D.3. In this study, only m and n are considered variable rock-electrical parameters for experimentation, while a and b remain fixed values. Among the inputs of d_{A}, a, b, and RW are experimentally determined constants, while POR and SW are determined based on the mineral volume content v. The sequential integration of data-driven and mechanism models enables embedding Archie's formula and accommodating variable rock-electrical parameters.

2.2. Staged PIAE

In conventional logging data interpretation, the interpretation of POR is typically derived using multi-mineral volume equations, followed by obtaining SW through Archie's formula. Therefore, the interpretation of SW is based on POR. The predictive order of POR and SW is considered, leading to the design of a staged reservoir parameter prediction model based on PIAE (staged PIAE), as illustrated in Fig. 1. The training of this model involves two stages: In the first stage, self-supervised training is conducted using the P1 component of PIAE, wherein water and oil neurons are employed to compute POR. Subsequently, in the second stage, the labels used for training include the logging data RT, mineral volume content, and POR obtained from the first stage. The parameters of the multi-mineral volume encoder e_{M} are transferred from the model in stage 1. And the Archie encoder e_{A} and decoder d_{A} are incorporated for continued training and predicting SW.

The staged PIAE incorporates expert experience into the model training process, employing distinct mechanism models for different processes and enabling more targeted prediction of reservoir parameters. In contrast to the staged PIAE, the end-to-end PIAE facilitates simultaneous prediction of multiple reservoir parameters. Both utilize the model architecture of auto-encoders, enabling them to undergo self-supervised training without reservoir parameter labels, thereby reducing the dependency on labels. The PIAE and staged PIAE also share an identical internal structure in different modules.

2.3. Loss function

Based on the supervision term of PIAE and staged PIAE, the loss function L_{data} is formulated as a weighted sum of Mean Squared Error (MSE), according to Eqs. (15) and (16), where the weights are the reciprocals of the standard deviation σ of the labels, as shown in Eq. (17). The model's attention is prioritized by assigning a higher weight to data with a more concentrated distribution, thereby facilitating a more comprehensive understanding of their distinctive features.

$$L_{\mathrm{data}} = \sum_i \frac{\mathrm{MSE}_i}{\sigma_i}, \tag{15}$$

$$\mathrm{MSE}_X = \frac{1}{N}\sum_{i=0}^{N}(X - X^*) \tag{16}$$

$$\sigma = \sqrt{\frac{1}{N}\sum_{i=0}^{N}(X - \overline{X})^2} \tag{17}$$

In traditional logging data interpretation research, a significant amount of domain knowledge has been accumulated. For the rock electrical parameters m and n in Archie's formula, it is generally believed that a reasonable range for m is 1.5–3, and n is typically set to 2. The constraints of m and n are incorporated into the loss function, aiming to ensure that the values of m and n align with empirical ranges as much as possible. The penalty term Eq. (18) is introduced, as outlined in Appendix B for its derivation. The final training loss function is given by Eq. (19), where λ denotes the weight of the penalty term.

$$L_{mn} = \sum_i f_{\mathrm{ReLU}}((1.5 - m_i)(3 - m_i) - \varepsilon) + \sum_i f_{\mathrm{ReLU}}\left((2 - n_i)^2 - \varepsilon\right) \tag{18}$$

$$Loss = (1 - \lambda)L_{\mathrm{data}} + \lambda L_{mn} \tag{19}$$

3. Case study

In this section, we demonstrate the effectiveness of the proposed PIAE method on a real-world logging dataset. Firstly, we compare the different model structures of multi-mineral volume encoders, including CNN, LSTM, and the parallel structure of CNN and LSTM (CNN-LSTM). Secondly, we introduce a trainable mechanism decoder and verify the effectiveness of the optimization algorithm. Thirdly, the effectiveness of adding the penalty term in the loss function to constrain the rock-electrical parameters is verified. Fourthly, we conduct a comparative analysis between the end-to-end and staged process, examining the applicability of both

approaches. Then, we test groups of the experiment in the extended dataset to verify the adaptability of the PIAE method. Finally, a comprehensive evaluation of the robustness of PIAE is presented under various noise conditions, specifically focusing on Gaussian noise and salt-and-pepper noise.

3.1. Dataset and evaluation metric

The experiment utilizes conventional logging data from a specific geology region. Based on the oil testing results and stratigraphic division, the reservoir data for this region were selected as the experimental dataset. Due to the tight sandstone reservoir nature, challenges such as low porosity, low permeability, complex pore structure, and poor petrophysical properties are present. Consequently, there are deviations between conventional interpretation results and core data.

The logging depth of this reservoir ranges from 2500 to 2800 m with a sampling interval of 0.125 m. The distribution of logging data is presented in Table 1, where inter_POR and inter_SW denote interpretation results, core_POR and core_SW denote core data. The dataset is combined with 55 wells, where 55 wells have core_POR and only 8 wells have core_SW. The amount of core data in each well ranges from 8 to 187. The interpretations of POR and SW are available for all wells and were derived by experts based on their experience and relevant geological materials.

A total of 53015 sets of well logging data samples were obtained by data pre-processing, as shown in Fig. 3, where DEN, CNL, AC, GR, and RT are taken as raw logging data. Considering the limited features of the original dataset and the sequential nature of logging data, the model design involves augmenting the dimensions through window slicing. The pre-processing workflow for slicing logging data needs to ensure the continuity of depth within the samples. This process first removes duplicate depths and sorts the remaining data to maintain the correct order of depths in the original features. Then, outliers are marked to avoid affecting the normalization process. Further, the slicing samples containing marked outliers are removed, and the continuity in each sample is checked to prevent discontinuities caused by missing data along the depth in the original dataset. This comprehensive process yields a dataset specific to a well, ensuring data integrity and continuity for subsequent analysis. The dataset does not need to be partitioned into training and testing sets because the proposed method is designed for self-supervised training without requiring reservoir parameter labels. Thus, all samples in the dataset are used for training, and the samples with core labels are tested. The prediction results (pre_POR, pre_SW) are compared with the core data and the interpreted results, followed by performance metrics evaluation.

Regression tasks commonly use evaluation metrics like Mean Absolute Error (MAE), Mean Absolute Percentage Error (MAPE), Mean Squared Error (MSE), and the coefficient of determination (R^2). While R^2 assesses trend consistency between labels and predictions, it is less suitable in this paper due to the discontinuous nature of core data, which serves as ground truth. Additionally, MSE is sensitive to significant errors. However, extreme values are avoided with our model's constraints on reservoir parameter predictions, making MAE and MSE performance broadly consistent. Thus, we evaluate model performance using MAE and MAPE, offering a comprehensive assessment of absolute and relative accuracy. As shown in Eqs. (20) and (21), MAE provides a straightforward measure of average error, while MAPE is scale-invariant and expresses errors as a percentage.

Table 1
Statistical analysis of data set.

	Amount	Mean	Std	Min	Max
DEN	53015	2.57	0.12	1.27	2.84
CNL	53015	21.62	6.47	2.47	94.61
AC	53015	230.10	20.20	177.50	341.39
GR	53015	98.92	20.52	37.52	241.80
RT	53015	27.61	69.31	1.16	2000.00
inter_POR	14036	8.76	2.90	0.10	18.82
inter_SW	12008	67.13	15.80	13.79	99.89
core_POR	3374	9.00	2.67	0.58	16.55
core_SW	486	43.83	11.66	19.08	82.79

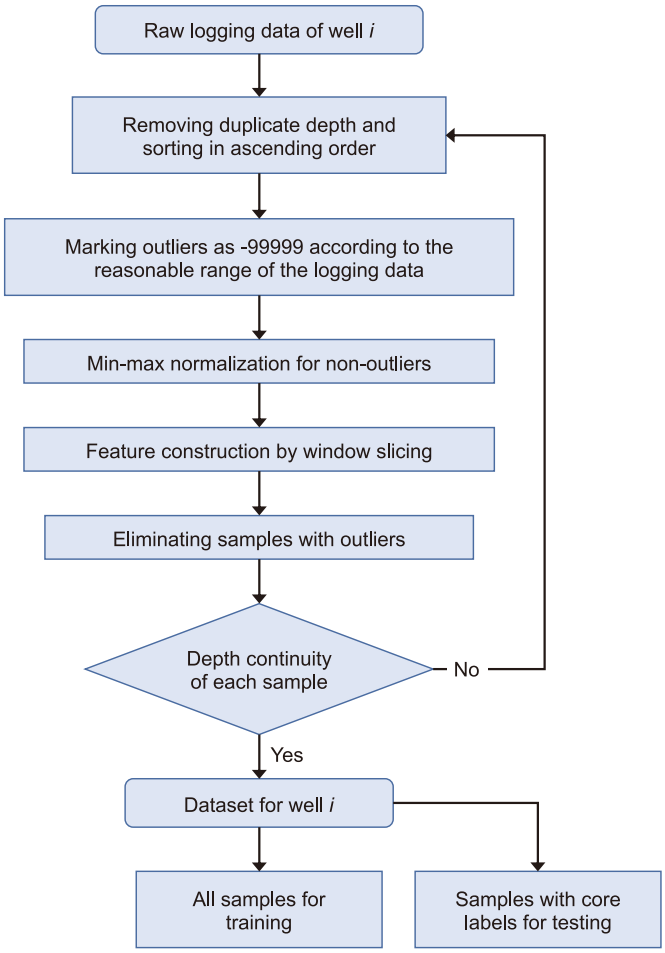

Fig. 3. Flow chart of data pre-processing.

$$\mathrm{MAE} = \frac{1}{n}\sum_{i=1}^{n}|y_i - \hat{y}_i| \tag{20}$$

$$\mathrm{MAPE} = \frac{1}{n}\sum_{i=1}^{n}\left|\frac{y_i - \hat{y}_i}{y_i}\right| \cdot 100\% \tag{21}$$

3.2. Implement details

The proposed model is built on PyTorch (Paszke et al., 2017), using the Adam optimizer with a learning rate 1×10^{-3} for updating the parameters. The batch size is set to 512. All experiments are conducted on the NVIDIA RTX 3090 GPU. For example,

training on a single well with 951 samples required approximately 7000 epochs, which took around 3 min to complete. We use the same hyper-parameter setting for the 55 wells in the dataset and train the model on each well individually.

3.3. Multi-mineral volume encoder based on CNN and LSTM

The first experiment evaluates the effect of different multi-mineral volume encoders in PIAE on well A. Two fundamental models, LSTM and CNN, were selected for investigation. They can extract features and capture sequential relationships among samples from different perspectives. Three models were configured: CNN, LSTM, and a parallel structure of CNN and LSTM (CNN-LSTM), with the specific network structures outlined in Appendix D.

The cross plot of POR and SW are illustrated in Fig. 4. The interpretation and prediction errors under three different encoder structures are presented in Table 3, with the core data serving as the ground truth. Additionally, the predictive performance of the reconstructed logging data for three sets of experiments is presented in Table 2.

The five reconstructed logging data are used for supervised training during the training process. The evaluation metrics in Table 2 show that CNN-LSTM outperforms LSTM and CNN in terms of prediction performance. Among them, CNN exhibits the weakest predictive performance. To ensure the reconstructed reservoir parameters satisfy primary physical constraints in PIAE, the accuracy of the reconstructed logging data is necessary. Therefore, theoretically, the predicted reservoir parameters POR and SW cannot be reliable when selected by the CNN-based multi-mineral volume encoder.

The training of reservoir parameters POR and SW is conducted unsupervised. According to the evaluation index presented in Table 3, all three models achieve predictions that are generally superior to the interpretation results. LSTM and CNN-LSTM prediction errors on the two reservoir parameters are close, and both models outperform the interpretation results. The predictive performance of POR is enhanced by 17.56% and 32.26% in terms of MAE and MAPE, respectively. The predictive performance of SW is improved by 45.53% and 49.17% on MAE and MAPE, respectively. The CNN demonstrates superior predictive capability for POR compared to the interpreted results, but a significant bias exists in the SW prediction.

Further insights can be gained from Fig. 4, where blue points represent interpreted results and orange points represent predicted results. The proximity of data points to the red dashed line signifies a better fit to core data. By comparing the results from the three sets

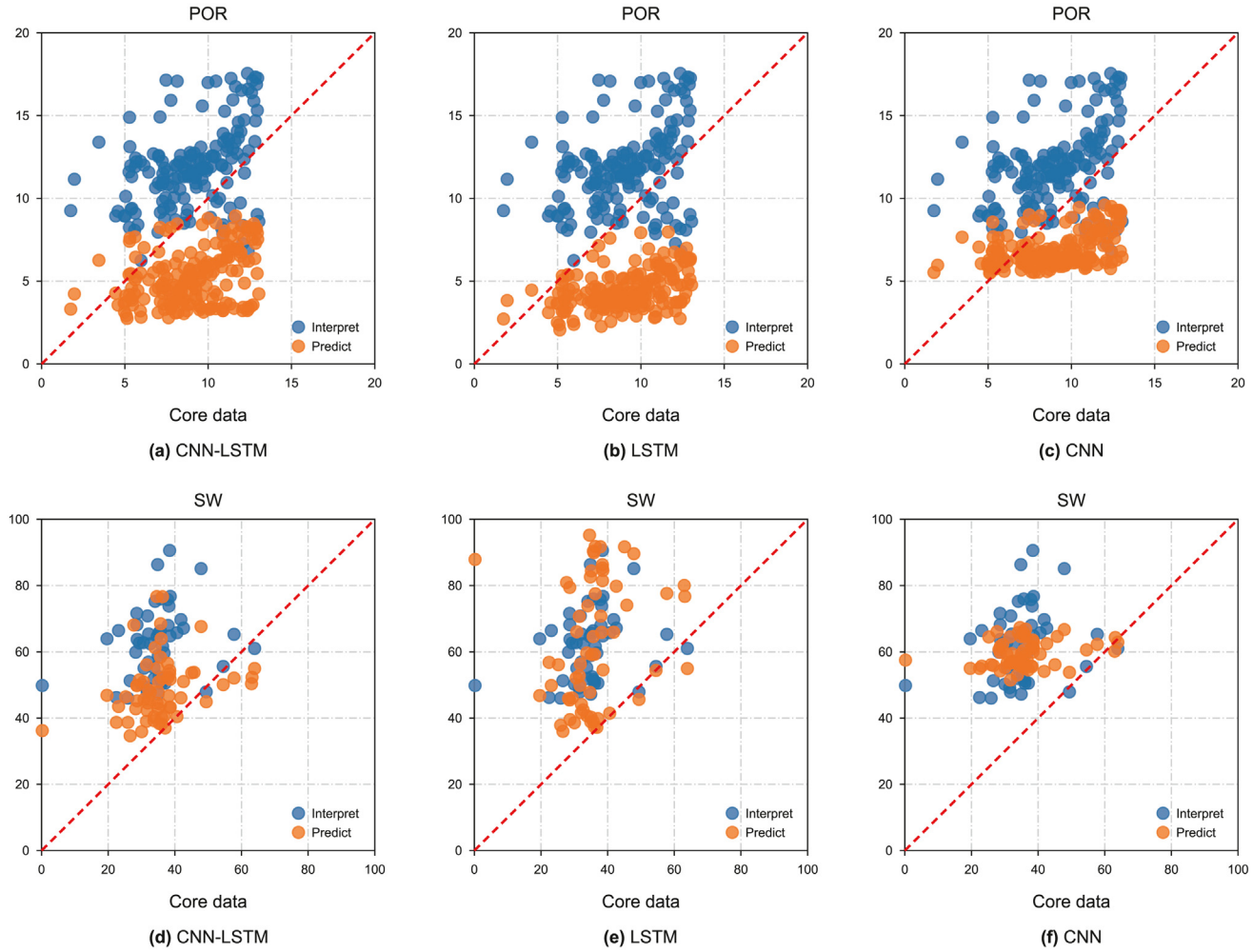

Fig. 4. Cross plots of POR and SW in different experiment settings. The X-axis represents the core data of POR or SW, and the *Y*-axis represents the interpreted result in blue or the predicted result in orange. The red dashed line represents the ideal result equal to the core data. **(a)**–**(c)** demonstrate the cross plots of POR, and **(d)**–**(f)** demonstrate the cross plots of SW.

Table 2
Error of reconstructed logging data in different multi-mineral volume encoders.

		CNN	LSTM	CNN-LSTM
DEN	MAE	0.057	0.053	0.027
	MAPE	0.022	0.021	0.011
CNL	MAE	2.114	1.753	1.745
	MAPE	0.104	0.081	0.078
AC	MAE	10.942	8.891	10.708
	MAPE	0.049	0.040	0.047
GR	MAE	18.373	17.081	10.224
	MAPE	0.251	0.217	0.121
RT	MAE	12.298	28.697	5.395
	MAPE	0.468	0.726	0.201
SUM	MAE	43.783	56.474	28.100
	MAPE	0.893	1.084	0.458

Table 3
Performance comparison between different multi-mineral volume encoders.

Well A	POR		SW	
	MAE	MAPE	MAE	MAPE
Interpretation error	3.36	47.42	26.97	82.94
CNN	3.16	33.24	52.45	157.18
LSTM	2.81	32.12	14.69	42.16
CNN-LSTM	2.77	32.23	14.77	42.52

of experiments, it is evident that the distribution of CNN's predicted results is more concentrated, while LSTM's predicted results exhibit a strong correlation with interpreted results. The predictive performance of the CNN-LSTM closely approximates that of the LSTM. However, it is noteworthy that the CNN-LSTM's predictions exhibit a more substantial alignment with the core data, as illustrated by their proximity to the red dashed line in Fig. 4. It suggests that CNN-LSTM's predictive outcomes exhibit a more pronounced fidelity to the core dataset.

Considering both the predictive performance of reconstructed logging data and the reservoir parameters POR and SW, CNN-LSTM stands out as the optimal model for the multi-mineral volume encoder.

3.4. Trainable mechanism decoder

Algorithm 1. Optimization algorithm of trainable mechanism decoder.

Input: $\boldsymbol{x} = [x^1, x^2, \cdots x^N] \in R^{N \times W}$
Initialization:
Initialize parameter ρ in the decoder d_M with fixed weight and set requires_grade as False;
Randomly initialize parameters θ and φ in encoders.
1: for epoch **do**:
2: Updating encoder parameters θ and φ as follows:

$$\min_{\theta,\varphi} \boldsymbol{Loss}$$

3: if early stop condition:
4: Set requires_grade as True
5: Updating parameters θ, φ and ρ as follows:

$$\min_{\theta,\varphi,\rho} \boldsymbol{Loss}$$

6: if early stop condition:
7: Break
8: End for

We introduce an optimization algorithm of a trainable mechanism decoder described in Algorithm 1. In PIAE, only the multi-mineral volume decoder d_M has parameters that can be updated by gradient descent. Thus, we use the algorithm to update ρ according to the logging data and obtain more suitable parameters for the well. The evaluation metrics are shown in Fig. 5, and the comparison results are shown in Fig. 6.

Comparing the evaluation metrics obtained by different optimization algorithms, the trainable mechanism decoder has better performance in the prediction of POR and SW, as shown in Fig. 5. Specifically, MAE and MAPE of predicted POR are reduced by 52.94% and 42.77%, respectively, and metrics of predicted SW decreased by 58.25% and 58.16%, respectively. Taking the dashed lines in Fig. 5 as the baseline, the prediction error of the trainable mechanism decoder is lower than the interpretation error. In contrast, the fixed mechanism decoder is higher than the interpretation error. It indicates that the fixed mechanism decoder cannot adapt when the initialized mechanism parameters do not conform to the logging data.

There is an abnormal prediction MAPE of SW in Fig. 5(b) with a value of 132.93%, which means that the value of core data is smaller than the error of the predicted result and core data. It could be caused by abnormally low values of core data or failure of model predictions. In these cases, the value of MAPE will be scaled up to be greater than 100%. In Fig. 6, the SW in the 2554–2558 m depth proves that the fixed mechanism decoder fails in predicting SW.

The above results show that the trainable mechanism decoder can better predict POR and SW. It is demonstrated that the mechanism framework and initial parameters constrain the solution space of the model. The mechanism parameters are adjusted based on the logging data during training, aiming to achieve a balance between logging data and mechanism model.

3.5. Rock-electrical parameters constraints

The effectiveness of constraints on rock-electrical parameters is verified by conducting experiments on the penalty term L_{mn} in the loss function. The distributions of m and n based on different loss functions are shown in Fig. 7, where the dashed lines denote the empirically reasonable range or value of m and n. The evaluation metrics of interpretation error and prediction error in different loss functions are listed in Table 4. Performance comparison based on different loss functions.

The effectiveness of L_{mn} is substantiated from two perspectives. Firstly, considering the empirical range for m of 1.5–2 and the empirical value for n of 2, the L_{mn} restricts the distribution of m and n within a reasonable range in Fig. 7. Additionally, the constrain

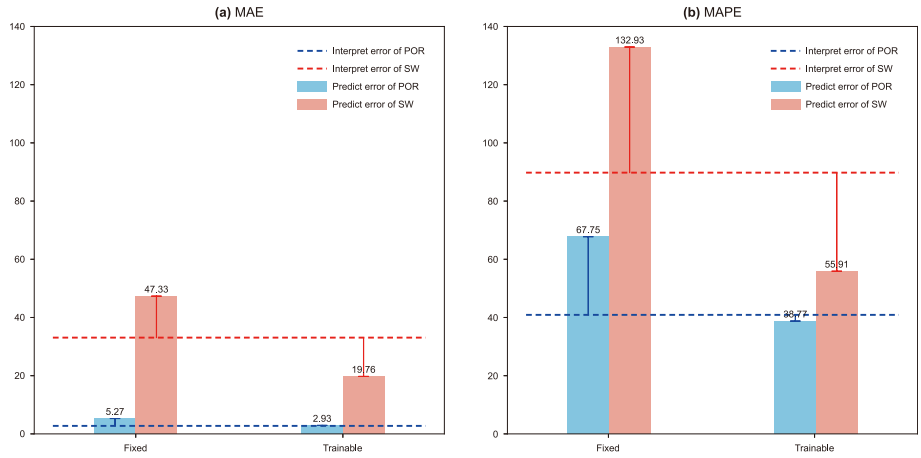

Fig. 5. The histogram of evaluation metrics in fixed and trainable mechanism decoder d_M. The core data serves as ground truth to obtain the metrics MAE and MAPE. The dashed line represents the interpretation error. The variation between the prediction error and the interpretation error is delineated.

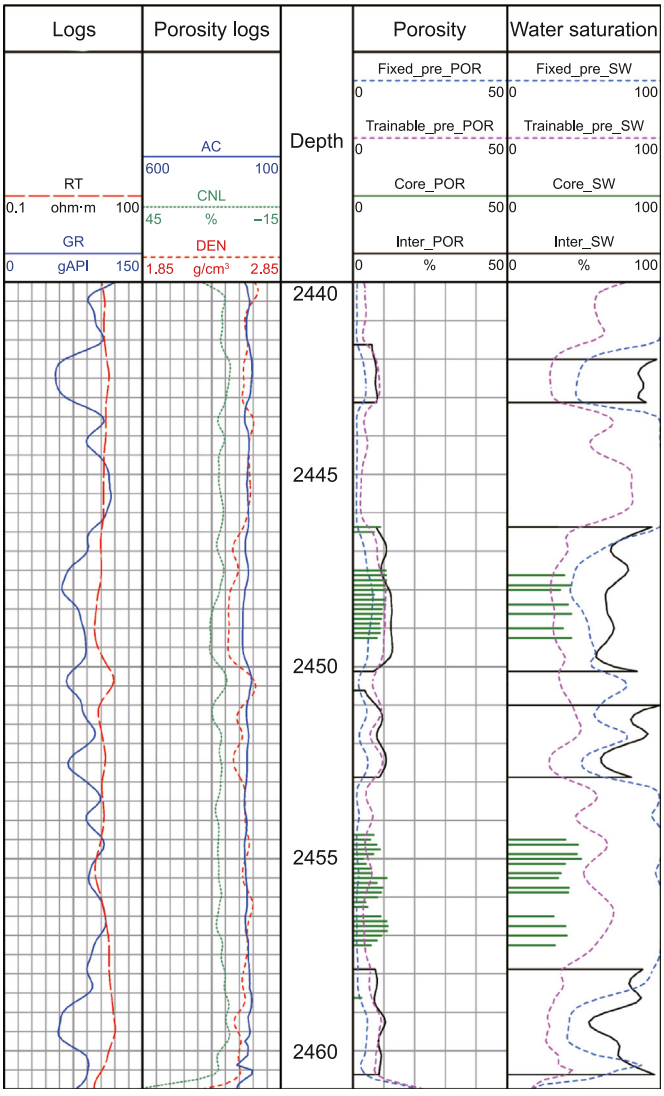

Fig. 6. Predictive results of POR and SW in fixed and trainable mechanism decoder.

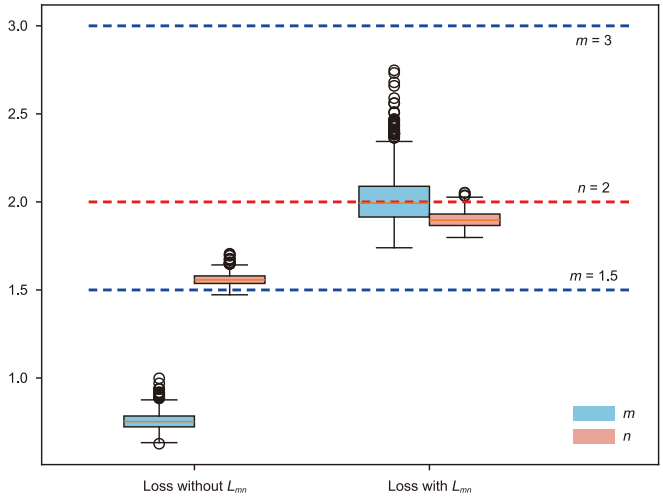

Fig. 7. Distributions of rock-electrical parameters m and n.The dashed lines denote the empirically reasonable range or value of m and n.

Table 4
Performance comparison based on different loss functions.

Well B	POR		SW	
	MAE	MAPE	MAE	MAPE
Interpretation error	2.30	29.65	19.23	43.11
Loss without L_{mn}	2.26	41.94	32.46	68.77
Loss with L_{mn}	2.30	43.28	9.41	19.26

Table 5
Performance comparison between end-to-end and staged process based on PIAE.

Well C		POR		SW	
		MAE	MAPE	MAE	MAPE
Interpretation error		3.30	58.77	18.71	62.30
Staged	Stage1	3.60	64.57	19.31	65.45
	Stage2	3.61	64.75	9.47	27.68
End-to-end		**2.82**	**52.41**	**7.10**	**21.15**

ensures that the model remains consistent with established knowledge while also allowing room for flexibility. This intuitive validation contributes significantly to enhancing our understanding and interpretation of results obtained by the method.

Secondly, regarding the prediction results, the MAE of POR

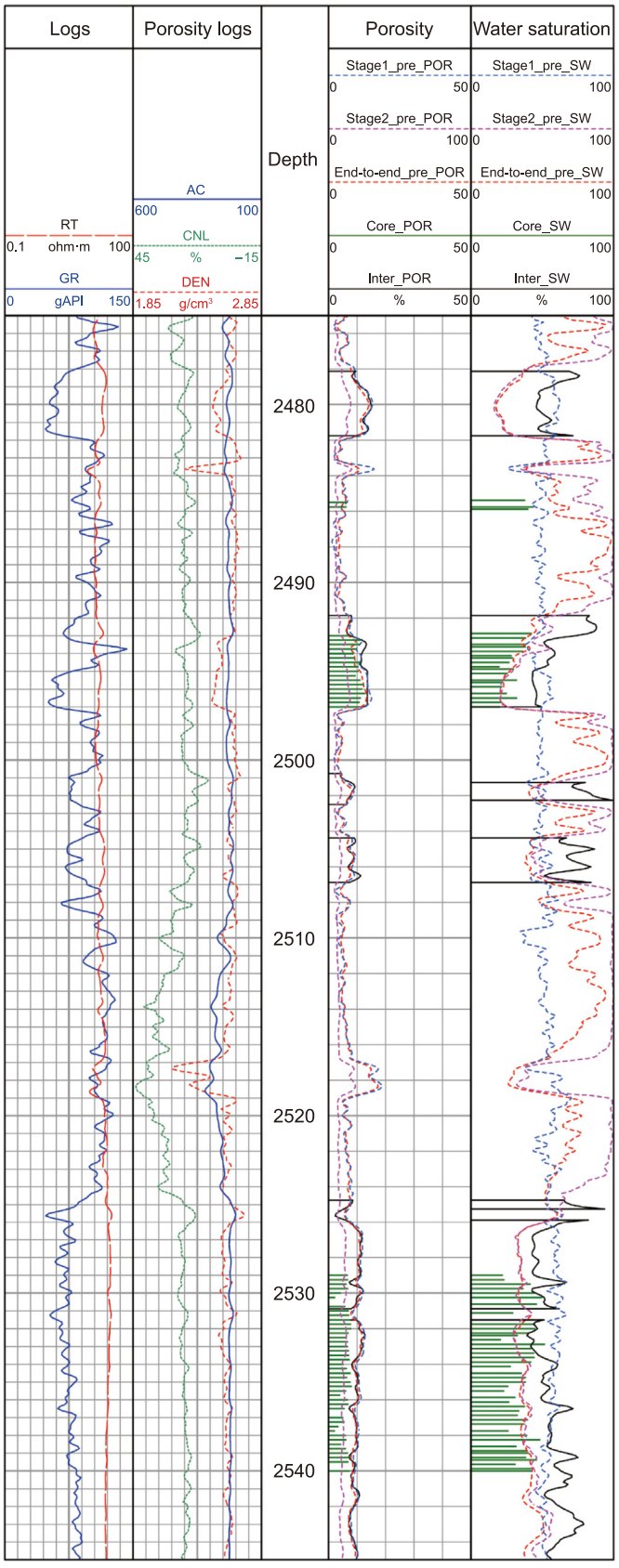

Fig. 8. Predictive results of POR and SW in end-to-end and staged processes based on PIAE.

remains consistent while the MAPE increases. The increase in MAPE indicates that the prediction errors mainly occur at depths with lower POR values and the interpretation errors mainly arise at depths with higher POR values. Thus, the performance on POR is consistent regardless of whether a penalty term is used. Additionally, the L_{mn} effectively reduces the prediction error for SW, achieving an error lower than the interpretation error. When POR remains unchanged while SW decreases, this further corroborates the efficacy of constraining m and n in Archie's formula.

3.6. End-to-end and staged process based on PIAE

In this experiment, the impact of different processes on the performance of predicted reservoir parameters is tested on well C. In traditional logging data interpretation, the POR is interpreted first, and then the SW is obtained based on the POR. Thus, this experiment explores whether the order in the traditional method is necessary for PIAE. Table 5 shows the interpretation and prediction errors of different methods, taking core data as the ground truth. The specific prediction results are illustrated in Fig. 8.

Regarding the two stages of the staged PIAE, the results demonstrate a similar predictive effect for POR in both stages. Additionally, there is a significant enhancement in the performance of SW after undergoing the second stage of training, resulting in a reduction of 50.96% and 57.71% in MAE and MAPE, respectively. The prediction SW of the first stage in Fig. 8 fluctuates in a small range near 50, which means the model is entirely invalid for predicting SW. It indicates that the multi-mineral volume decoder in the first stage primarily serves to constrain POR, and the Archie decoder in the second stage is primarily utilized to constrain SW.

The effectiveness of the two decoders can be explained from the perspective of model architecture. The mineral response matrix for logging data is constructed from Table A.1, which serves as the initialization parameters for the fully connected layers and is utilized to constrain the model training. Heatmaps depicting the correlations of each neuron in the data representation layer are illustrated, as shown in Fig. A.1. The strong correlation between the initialization vectors of water and oil neurons indicates that the logging response module cannot differentiate between these two neurons, implying limited constraints on the prediction of SW.

Further comparing the prediction performance of the two processes, end-to-end PIAE achieves a lower prediction error on both POR and SW. Thus, it can effectively integrate the constraints of different mechanism models and balance the influence of different mechanism decoders under the supervision of actual logging data to obtain more realistic inversion results.

3.7. Extended testing on multiple wells

We tested five groups of experiments on 55 wells, and the models for each well were trained separately. The specific experimental settings are shown in Table 6. Figs. 9 and 10 are derived based on the statistical analysis of experimental results obtained from multiple wells, with 55 wells contributing to the POR results and 8 wells contributing to the SW results. Figs. 9 and 10 illustrate three distinct types of errors. Two sets of prediction errors are computed, taking interpretation results and core data as the ground truth. The third set measures the deviation of prediction errors from interpretation errors by considering core data as the ground truth. A positive change indicates that the interpretation result is closer to the core data, while a negative change suggests that the prediction result is closer to the core data. The red dashed line represents that the MAE variation is 0.8 and the MAPE variation is 5. The number of wells falling below this threshold is tallied, as illustrated in Table 6.

Table 6
The count of wells with error variation that meet the eligibility criteria in different experiment settings.

Experiment	Multi-mineral encoder	Multi-mineral decoder	Process	MAPE <5%		MAE <0.8	
				POR	SW	POR	SW
A	CNN-LSTM	Trainable	End-to-end	**34**	**6**	**38**	**4**
B	CNN-LSTM	Fixed	End-to-end	23	4	26	3
C	LSTM	Trainable	End-to-end	29	4	33	3
D	CNN	Trainable	End-to-end	22	1	23	1
E	CNN-LSTM	Trainable	Staged	31	4	39	3

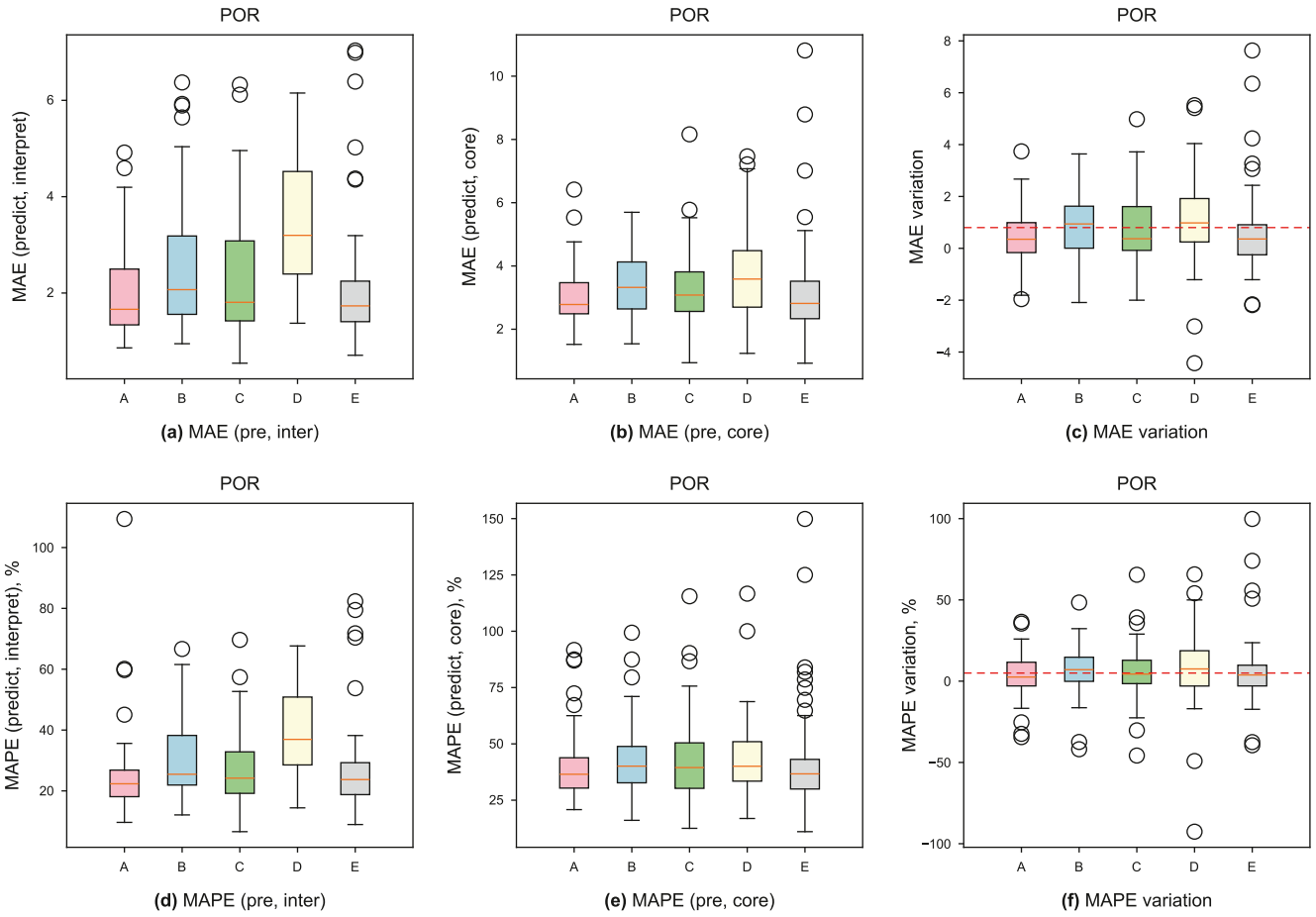

Fig. 9. Box plots of the error and error variation in different experiment settings. The red dashed line represents that the MAE variation is 0.8 and the MAPE variation is 5. The data of POR is collected from 55 wells. The box represents the interquartile range, which contains the middle 50% of the data. The line inside the box indicates the median value, while the whiskers show the minimum and maximum values within a specific range, and the hollow circles represent outliers in the dataset.

The results depicted in Figs. 9 and 10 demonstrate minimal overall disparity among the five experimental groups. However, it is worth noting that experiment D exhibits a higher error rate than other experiments, suggesting that CNN may not be suitable for logging data when employed as an encoder. Conversely, both experiment A and experiment E yield more effective outcomes. Experiment especifically showcases a greater concentration of results but also reveals a broader distribution of anomalies. This observation indicates that the end-to-end process can be adapted to logging data from various wells with enhanced generalization capabilities and superior mobility compared to the staged process. The comparison of the results between experiment A and experiment B reveals that the data distribution range in experiment B is wider, indicating that the trainable mechanism model can yield more precise and stable prediction outcomes.

The data in Table 6 illustrates the number of wells exhibiting error variations below 5% MAPE and 0.8 MAE thresholds. The findings indicate that group A had the most favorable experimental effect. The POR prediction results revealed that 61.82% and 69.09% of wells satisfied the MAPE and MAE criteria, respectively. Regarding the SW prediction results, it was found that 75% and 50% of Wells met the MAPE and MAE conditions correspondingly. Through verification using multiple well data, it can be concluded that the PIAE method adequately fulfills the requirements for automatic interpretation without necessitating reservoir parameter labels.

3.8. Robustness of PIAE

In this section, we conduct two experiments to evaluate the

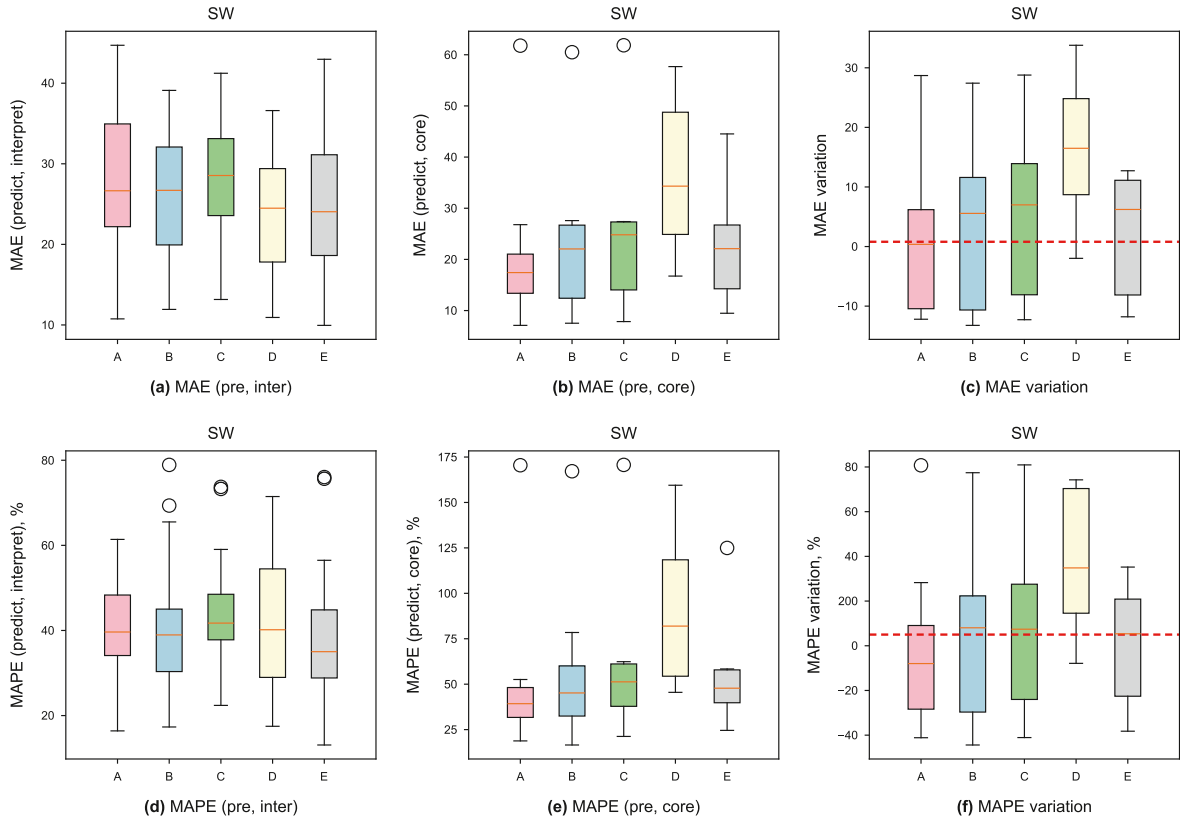

Fig. 10. Box plots of the error and error variation in different experiment settings. The red dashed line represents that the MAE variation is 0.8 and the MAPE variation is 5. The data of SW is collected from 8 wells. The box represents the interquartile range, which contains the middle 50% of the data. The line inside the box indicates the median value, while the whiskers show the minimum and maximum values within a specific range, and the hollow circles represent outliers in the dataset.

Table 7
Performance comparison between different noisy data.

Well A		POR		SW	
		MAE	MAPE	MAE	MAPE
Interpretation error		2.27	39.09	19.66	58.40
Prediction error		2.61	**37.62**	**15.92**	**40.17**
Gaussian	$\sigma = 0.1$	2.67	**38.31**	**16.77**	**42.87**
	$\sigma = 0.2$	2.91	40.46	**18.38**	**48.65**
	$\sigma = 0.3$	3.58	47.81	22.28	60.09
Salt-and-Pepper	$p = 10\%$	2.65	**38.41**	**15.44**	**39.90**
	$p = 20\%$	2.84	40.64	**15.75**	**39.36**
	$p = 30\%$	2.96	43.73	**16.15**	**39.96**

robustness of the PIAE, focusing on its performance under different noise conditions. Firstly, we test the model's error under varying levels of Gaussian noise, with different variances ($\sigma = 0.1, 0.2, 0.3$) added to the input data to simulate different levels of noise in well logging measurements. Secondly, we evaluate the model's robustness to salt-and-pepper noise, which randomly alters different proportions ($p = 10\%, 20\%, 30\%$) of the input data to either the maximum or minimum value. This type of noise simulates the presence of outliers or anomalies in well logging data.

The experimental results, summarized in Table 7, show that as the Gaussian and salt-and-pepper noise level increased, the model's prediction error also increased. However, the model's sensitivity to the two types of noise has distinct differences. The PIAE shows higher sensitivity to Gaussian noise. When the variance of the Gaussian noise increased to 0.3, the prediction error exceeded the interpretive error, indicating sharp performance degradation under high.

Gaussian noise conditions. In contrast, the model is more robust to salt-and-pepper noise. Even as the proportion of salt-and-pepper noise increased to 30%, the reduction in predictive performance is relatively small, with the prediction for SW remaining within acceptable error margins. These observations suggest that the PIAE model's robustness is influenced by the type and level of noise present in the input data. The model's higher sensitivity to Gaussian noise is attributed to its statistical characteristics, which uniformly affect all data, whereas salt-and-pepper noise introduces isolated anomalies that the PIAE model can better handle due to its feature construction process involving window slicing, which help mitigate the impact of outliers.

Table A.1
Logging mineral response values.

	DEN	CNL	AC	GR
Quartz	2.65	−6	55	0
Calcite	2.71	0	47.5	0
Mica	2.8	20	65	270
Chlorite	2.76	52	60	220
Illite	2.5	36	100	270
Kaolinite	2.51	40	80	110
Montmorillonite	2.02	40	110	220
Water	1	100	189	0
Oil	0.8	100	200	0

4. Conclusions

This paper investigates the integration of data-driven and mechanism models for reservoir parameter prediction. We introduce the PIAE, a model based on the auto-encoder architecture that integrates mechanism models into the network structure, loss function, and training process. Various forms of prior information from the geophysical logging domain are skillfully incorporated into the different aspects of the machine learning framework. The model balances mechanism and data-driven approaches through iterative training of neural networks. The validity of the PIAE is tested using logging data from an actual tight sandstone reservoir, leading to several key conclusions.

(1) Precision Improvement: Experimental evidence demonstrates that the PIAE achieves superior performance compared to traditional interpretation methods without relying on labels for POR and SW. It signifies the potential for cost-effective and accurate reservoir parameter predictions while ensuring the predicted results adhere to fundamental physical constraints.
(2) Adaptability and Interpretability: The flexibility and trainability of the embedded mechanism model parameters allow for adjustments based on varying geological settings, making the method highly adaptable and versatile. Moreover, experts can manually adjust the parameters to correct unreasonable deviations in the predictions, enhancing the model's interpretability.
(3) Generalization: The PIAE is trained using self-supervised methods without reservoir parameter labels and can deal with new areas where labeled training samples are scarce. Thus, the method facilitates generalization across diverse datasets.
(4) Robustness: The model's design, particularly the slicing feature during data preprocessing, plays a significant role in minimizing the influence of outliers, thus maintaining predictive accuracy in the presence of noise.

This method possesses both theoretical significance and practical value. It ensures high precision and mitigates expenses, providing substantial support for the comprehensive interpretation of logging data. However, the current design of PIAE is specifically tailored to predict POR and SW, which may lead to scalability issues when extending the model to predict other parameters. The model architecture would need to be adjusted according to the mechanism of the target parameter, with the complexity of this adjustment correlating to the complexity of the mechanism model.

Future work will focus on addressing the scalability issues by developing a more flexible model architecture that can easily adapt to additional parameters. This will involve creating modular components within the model, allowing for adjustments based on the mechanism models of different parameters.

CRediT authorship contribution statement

Meng-Lu Kang: Writing – original draft, Visualization, Methodology, Data curation, Conceptualization. **Jun Zhou:** Writing – review & editing, Funding acquisition, Conceptualization. **Juan Zhang:** Supervision, Resources. **Li-Zhi Xiao:** Writing – review & editing, Funding acquisition, Conceptualization. **Guang-Zhi Liao:** Writing – review & editing. **Rong-Bo Shao:** Writing – review & editing, Supervision, Formal analysis. **Gang Luo:** Writing – review & editing, Formal analysis.

Declaration of competing interest

The authors declare that they have no known competing financial interests or personal relationships that could have appeared to influence the work reported in this paper.

Acknowledgement

This work was supported by National Key Research and Development Program (2019YFA0708301), National Natural Science Foundation of China (51974337), the Strategic Cooperation Projects of CNPC and CUPB (ZLZX2020-03), Science and Technology Innovation Fund of CNPC (2021DQ02-0403), Open Fund of Petroleum Exploration and Development Research Institute of CNPC (2022-KFKT-09).

Nomenclature

DEN	Density log
CNL	Compensating neutron log
AC	Acoustic log
GR	Gamma ray
RT	Formation resistivity
RW	Formation water resistivity
POR	Porosity
SW	Water saturation
GRU	Gated Recurrent Units
MLP	Multi-layer perceptron
CNN	Convolutional Neural Network
LSTM	Long Short-Term Memory
CNN-LSTM	The parallel structure of CNN and LSTM
PIAE	Physically Informed Auto-Encoder
Staged PIAE	Staged reservoir parameter prediction model based on PIAE
$d_{\mathrm{M}}(x;\rho)$	Multi-mineral volume decoder
$e_{\mathrm{M}}(x;\theta)$	Multi-mineral volume encoder
$d_{\mathrm{A}}(x)$	Archie decoder
$e_{\mathrm{A}}(x;\varphi)$	Archie encoder
ρ,θ,φ	Trainable parameters of modules
W	Window length
N	Number of features
M	Number of mineral components
a,b,m,n	Rock-electrical parameters
pre	Prediction results
core	Core data
inter	Interpreted results

Appendices

A. Mineral response matrix for reservoir parameter learning module

Reference to Table "Logging Characteristics of Major Sedimentary Rock Minerals" in "Logging Data Processing and Comprehensive Interpretation" (Yong and Zhang, 2007), coefficient matrix is obtained and is used for predefining weights of multi-mineral decoder d_M. Subsequently, the decoder does not perform weight updates to enforce physical constraints. The specific coefficient matrix is presented in Table A.1. Furthermore, the correlation between well log response vectors for each mineral component was computed, and the correlation heatmap is shown in Fig. A.1.

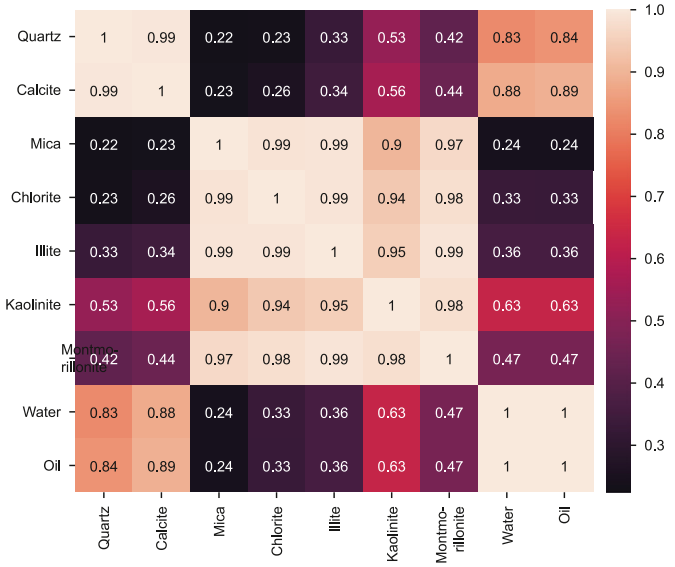

Fig. A.1. Heatmap of the correlation of logging mineral response vectors.

B. Loss function penalty term derivation

Assuming a constrained range (a, b) for the predicted value $\hat{y}$, we define a constraint function as follows:

$$G(\hat{y}) = (a - \hat{y})(b - \hat{y}) \tag{B.1}$$

When $\hat{y}$ lies within the interval (a, b), $G(\hat{y}) < 0$; when $\hat{y}$ is outside the interval (a, b), $G(\hat{y}) > 0$. Based on Eq. (B.1), a penalty term is constructed within the loss function:

$$L_{\hat{y}} = f_{\mathrm{ReLU}}(G(\hat{y}) - \varepsilon) \tag{B.2}$$

where ε represents the permissible error range, and f_{ReLU} stands for the Rectified Linear Unit (ReLU) activation function which is a commonly used activation function in artificial neural networks. ReLU function is typically defined as

$$f_{\mathrm{ReLU}}(x) = \max(x, 0) = \begin{cases} 0, x < 0 \\ x, x \geq 0 \end{cases} \tag{B.3}$$

This penalty term is designed to ensure that $L_G = 0$ when $\hat{y}$ falls within the interval $(a - \varepsilon_a, b - \varepsilon_b)$, and $L_G > 0$ when $\hat{y}$ is outside this interval. Moreover, the magnitude of L_G increases with a larger deviation from the interval $(a - \varepsilon_a, b - \varepsilon_b)$. The range of values for m is set to (1.5, 3), with n fixed at 2. Substituting these values into Eq. (B.2), the penalty terms for constraining m and n are as follows:

$$L_{mn} = \sum_i f_{\mathrm{ReLU}}((1.5 - m_i)(3 - m_i) - \varepsilon) + \sum_i f_{\mathrm{ReLU}}\left((2 - n_i)^2 - \varepsilon\right) \tag{B.4}$$

C. Hyper-parameters selection of PIAE

To ensure optimal performance, we conduct a grid search across a predefined range of critical parameters, including learning rate, model architecture, and weight λ in loss, as shown in Table C.1. The grid search involved systematically testing all possible combinations of these parameters to identify the configuration that minimizes the loss function and enhances model convergence.

Table C.1
Optimization of hyper-parameters in PIAE.

Parameters	Search range	Optimal setting
Learning rate	1×10^{-4}–1×10^{-2}	1×10^{-3}
CNN kernel size	2–5	3
LSTM hidden size	20–50	30
Weight λ in loss	0.1–0.4	0.2

D. Model structure of PIAE

The model architectures for the multi-mineral volume encoder, multi-mineral volume decoder, and Archie encoder in the PIAE are specified in Table D.1, Table D.2 and Table D.3.

Table D.1
Multi-mineral volume encoder $e_M(x; \theta)$.

CNN	
(0)	Conv1d (21, 5, kernel_size = (3), stride = (1))
(1)	BatchNorm1d (5, eps = 1e−05)
(2)	LeakyReLU ()
(3)	Dropout (p = 0.25)
(4)	Conv1d (5, 10, kernel_size = (3), stride = (1))
(5)	BatchNorm1d (10, eps = 1e-05)
(6)	LeakyReLU ()
(7)	Dropout (p = 0.25)
(8)	MaxPool1d (kernel_size = 3, stride = 2, padding = 1)
(9)	Flatten (start_dim = 1, end_dim = −1)
(10)	Linear (in_features = 30, out_features = 60)
(11)	Tanh ()
LSTM	
(0)	LSTM (5, 30)
(1)	Flatten (start_dim = 1, end_dim = −1)
(2)	Linear (in_features = 630, out_features = 320)
(3)	LeakyReLU (negative_slope = 0.2)
(4)	Linear (in_features = 320, out_features = 60)
(5)	Tanh ()
(6)	Linear (in_features = 120, out_features = 60)
(7)	Tanh ()
CNN-LSTM	
(0)	CNN (21, 60)
(1)	LSTM (5, 60)
(2)	Linear (in_features = 120, out_features = 60)
(3)	Tanh ()

Table D.2
Multi-mineral volume decoder $d_M(x; \rho)$.

(0)	Linear (in_features = 60, out_features = 9)
(1)	Softmax ()
(2)	Linear (in_features = 9, out_features = 4, bias = False)

Table D.3
Archie encoder $e_A(x;\varphi)$.

(0)	Linear (in_features = 42, out_features = 16)
(1)	LeakyReLU ()
(2)	Linear (in_features = 16, out_features = 32)
(3)	LeakyReLU ()
(4)	Linear (in_features = 32, out_features = 16)
(5)	LeakyReLU ()
(6)	Linear (in_features = 16, out_features = 2)

References

An, P., Cao, D.P., Zhao, B.Y., Yang, X.L., Zhang, M., 2019. Reservoir physical parameters prediction based on LSTM recurrent neural network. Prog. Geophys. 34, 1849–1858. https://doi.org/10.6038/pg2019CC0366 (in Chinese).

Archie, G., 1942. The electrical resistivity log as an aid in determining some reservoir characteristics. Transactions of the AIME 146, 54–62. https://doi.org/10.2118/942054-G.

Archie, G.E., 1947. Electrical resistivity an aid in core-analysis interpretation1. AAPG (Am. Assoc. Pet. Geol.) Bull. 31, 350–366. https://doi.org/10.1306/3D93395C-16B1-11D7-8645000102C1865D.

Chen, Y.T., Huang, D., Zhang, D.X., Zeng, J.S., Wang, N.Z., Zhang, H.R., Yan, J.Y., 2021. Theory-guided hard constraint projection (hcp): a knowledge-based data-driven scientific machine learning method. J. Comput. Phys. 445, 110624. https://doi.org/10.1016/j.jcp.2021.110624.

Chen, Y.T., Zhang, D.X., 2020. Physics-constrained deep learning of geomechanical logs. IEEE Trans. Geosci. Rem. Sens. 58, 5932–5943. https://doi.org/10.1109/TGRS.2020.2973171.

Doan, N.a.K., Polifke, W., Magri, L., 2020. Physics-informed echo state networks. Journal of Computational Science 47, 101237. https://doi.org/10.1016/j.jocs.2020.101237.

Dong, S.Q., Zhong, Z.H., Cui, X.H., Zeng, L.B., Yang, X., Liu, J.J., Sun, Y.M., Hao, J.R., 2023a. A deep kernel method for lithofacies identification using conventional well logs. Petrol. Sci. 20, 1411–1428. https://doi.org/10.1016/j.petsci.2022.11.027.

Dong, S.Q., Sun, Y.M., Xu, T., Zeng, L.B., Du, X.Y., Yang, X., Liang, Y., 2023b. How to improve machine learning models for lithofacies identification by practical and novel ensemble strategy and principles. Petrol. Sci. 20, 733–752. https://doi.org/10.1016/j.petsci.2022.09.006.

Gao, L., Xie, R.H., Xiao, L.Z., Wang, S., Xu, C.Y., 2022. Identification of low-resistivity-low-contrast pay zones in the feature space with a multi-layer perceptron based on conventional well log data. Petrol. Sci. 19, 570–580. https://doi.org/10.1016/j.petsci.2021.12.012.

Gers, F.A., Schmidhuber, J., Cummins, F., 2000. Learning to forget: continual prediction with lstm. Neural Comput. 12, 2451–2471. https://doi.org/10.1162/089976600300015015.

Han, S., Pan, B.Z., 2010. Method for determining the cementation index m of pore reservoir and its influencing factors. Petroleum Geophysics 16–19 (in Chinese).

Haro, C.F., 2010. The equations archie forgot: anisotropy of the rocks. SPE Reservoir Eval. Eng. 13, 823–836. https://doi.org/10.2118/123913-PA.

Hochreiter, S., Schmidhuber, J., 1997. Long short-term memory. Neural Comput. 9, 1735–1780. https://doi.org/10.1162/neco.1997.9.8.1735.

Karniadakis, G.E., Kevrekidis, I.G., Lu, L., Perdikaris, P., Wang, S., Yang, L., 2021. Physics-informed machine learning. Nature Reviews Physics 3, 422–440. https://doi.org/10.1038/s42254-021-00314-5.

Kennedy, W.D., Herrick, D.C., 2012. Conductivity models for archie rocks. Geophysics 77, WA109–WA128. https://doi.org/10.1190/geo2011-0297.1.

Lecun, Y., Bottou, L., Bengio, Y., Haffner, P., 1998. Gradient-based learning applied to document recognition. Proc. IEEE 86, 2278–2324. https://doi.org/10.1109/5.726791.

Li, Y.W., Li, Z.J., Shao, L.F., Tian, F.C., Tang, J.Z., 2023. A new physics-informed method for the fracability evaluation of shale oil reservoirs. Coal Geol. Explor. 51. https://doi.org/10.12363/issn.1001-1986.23.02.0106 (in Chinese).

Liao, G.Z., Li, Y.Z., Xiao, L.Z., Qin, Z.J., Hu, X.Y., Hu, F.L., 2020. Prediction of microscopic pore structure of tight reservoirs using convolutional neural network model. Petroleum Science Bulletin 5, 26–38. https://doi.org/10.3969/j.issn.2096-1693.2020.01.003 (in Chinese).

Luo, G., Xiao, L.Z., Liao, G.Z., Luo, S.H., Shao, R.B., Zhou, J., Li, G.J., Hou, S.L., Wu, J.W., 2022. Multi-level reservoir identification with logs based on machine learning. In: SPWLA 63rd Annual Logging Symposium. OnePetro. https://doi.org/10.30632/SPWLA-2022-0114.

Paszke, A., Gross, S., Chintala, S., Chanan, G., Yang, E., DeVito, Z., Lin, Z., Desmaison, A., Antiga, L., Lerer, A., 2017. Automatic Differentiation in Pytorch.

Rao, C.P., Sun, H., Liu, Y., 2020. Physics-informed deep learning for incompressible laminar flows. Theoretical and Applied Mechanics Letters 10, 207–212. https://doi.org/10.1016/j.taml.2020.01.039.

Shao, R.B., Xiao, L.Z., Liao, G.Z., Zhou, J., Li, G.J., 2022a. A reservoir parameters prediction method for geophysical logs based on transfer learning. Chin. J. Geophys. 65, 796–808. https://doi.org/10.6038/cjg2022P0057 (in Chinese).

Shao, R.B., Xiao, L.Z., Liao, G.Z., Shi, Y.Q., Zhou, J., Li, G.J., Hou, X.L., 2022b. Multitask learning based reservoir parameters prediction with geophysical logs. Chin. J. Geophys. 65, 1883–1895. https://doi.org/10.6038/cjg2022P0177 (in Chinese).

Song, H., Chen, W., Li, M.J., Wang, H.Y., 2019. A method to predict reservoir parameters based on convolutional neural network-gated recurrent unit (cnn-gru). Petroleum Geology and Recovery Efficiency 26, 73–78. https://doi.org/10.13673/j.cnki.cn37-1359/te.2019.05.009 (in Chinese).

Sun, J.G., 2007. Archie's formula: historical background and earlier debates. Prog. Geophys. 22, 472–486 (in Chinese).

Szegedy, C., Liu, W., Jia, Y.Q., Sermanet, P., Reed, S., Anguelov, D., Erhan, D., Vanhoucke, V., Rabinovich, A., 2015. Going deeper with convolutions. In: 2015 Ieee Conference on Computer Vision and Pattern Recognition (Cvpr), Ieee, New York, pp. 1–9. https://doi.org/10.1109/cvpr.2015.7298594.

Tang, J.Z., Fan, B., Xiao, L.Z., Tian, S.C., Zhang, F.S., Zhang, L.Y., Weitz, D., 2021. A new ensemble machine-learning framework for searching sweet spots in shale reservoirs. SPE J. 26, 482–497. https://doi.org/10.2118/204224-PA.

Wang, J., Cao, J.X., You, J.C., Liu, J., Zhou, X., 2020. Prediction of reservoir porosity, permeability, and saturation based on a gated recurrent unit neural network. Geophys. Prospect. Pet. 59, 616–627. https://doi.org/10.3969/j.issn.1000-1441.2020.04.012.

Xiao, L.Z., 2022. The fusion of data-driven machine learning with mechanism models and interpretability issues. Geophys. Prospect. Pet. 61, 205–212. https://doi.org/10.3969/j.issn.1000-1441.2022.02.002 (in Chinese).

Yang, K.B., Wang, J.F., Ma, F.Q., Tang, H.Y., Pan, X.F., 2018. Analysis and countermeasures about applicable conditions of archie's formula. Natural Gas and Oil 36, 58–63. https://doi.org/10.3969/j.issn.1006-5539.2018.02.010 (in Chinese).

Yong, S.H., Zhang, C.M., 2007. Logging Data Processing and Comprehensive Interpretation. China University of Petroleum Press, Dongying, pp. 447–449.

Zhang, Z.S., 2020. Theoretical roots of archie formulas. Prog. Geophys. 35, 1514–1522. https://doi.org/10.6038/pg2020DD0408 (in Chinese).

Zhao, X.Z., Jin, F.M., Liu, X.W., Zhang, Z., Cong, Z.Y., Li, Z.J., Tang, J.Z., 2022. Numerical study of fracture dynamics in different shale fabric facies by integrating machine learning and 3-d lattice method: a case from cangdong sag, bohai bay basin, China. J. Petrol. Sci. Eng. 218, 110861. https://doi.org/10.1016/j.petrol.2022.110861.